Modelling the Flow Behaviour, Recrystallisation and Crystallographic Texture in Hot Deformed Fe-30wt%Ni Austenite

M.F. Abbod[1], C.M. Sellars[2], P. Cizek[3], D.A. Linkens[4], M. Mahfouf[4]

[1] School of Engineering and Design, Brunel University, Uxbridge UB8 3PH, UK
[2] Department of Engineering Materials, The University of Sheffield, Mappin Street, Sheffield S1 3JD, UK
[3] Centre for Material and Fibre Innovation, Deakin University, Pigdons Road, Geelong, Victoria 3217, Australia
[4] Department of Automatic Control and System Engineering, The University of Sheffield, Mappin Street, Sheffield S1 3JD, UK

Abstract: The present work describes a hybrid modelling approach developed for predicting the flow behaviour, recrystallisation characteristics and crystallographic texture evolution in a Fe-30wt%Ni austenitic model alloy subjected to hot plane strain compression. A series of compression tests were performed at temperatures between 850 and 1050ºC and strain rates between 0.1 and 10 s^{-1}. The evolution of grain structure, crystallographic texture and dislocation substructure was characterised in detail for a deformation temperature of 950ºC and strain rates of 0.1 and 10 s^{-1}, using electron backscatter diffraction and transmission electron microscopy. The hybrid modelling method utilises a combination of empirical, physically-based and neuro-fuzzy models. The flow stress is described as a function of the applied variables of strain rate and temperature using an empirical model. The recrystallisation behaviour is predicted from the measured microstructural state variables of internal dislocation density, subgrain size and misorientation between subgrains using a physically-based model. The texture evolution is modelled using artificial neural networks.

Keywords: thermomechanical processing, physically-based modelling, neuro-fuzzy modelling, stress-strain behaviour, microstructure, recrystallisation, texture.

1. Introduction

It is well known that the microstructure of materials such as steel plays a vital role in dictating the deformation behaviour during thermomechanical processing. The microstructure of the parent austenite also determines the final transformed microstructure, and hence the final properties. Consequently, the development of physically-based models of microstructural evolution during thermomechanical processing of metallic materials requires knowledge of the internal state variables, such as grain structure, crystallographic texture and dislocation substructure, over a range of processing conditions. A Fe-30wt%Ni based alloy has recently been shown to act as a good model material for investigation of hot deformation of austenite in conventional carbon-manganese steels [1]. This alloy has a stable austenitic structure down to room temperature, allowing the high temperature deformation structure to be readily characterized following a rapid cool after deformation [2]. This alloy is also believed to have comparable stacking fault energy to that of carbon steels, thus implying that the deformation response should be comparable [3].

When developing a model to predict material behaviour, the ultimate aim of modelling is to provide the tools that can be extended to all conditions and for any material. At the current status, physically-based modelling is difficult to apply to such extended conditions and materials. Extending the range of application requires carrying out a considerable amount of experimental research, which is a very time-consuming process. Therefore, it is desirable to develop a modelling tool to be used for prediction under extended deformation conditions and for different types of material. The combination of physical knowledge and black-box modelling, termed hybrid modelling, is an attractive way for further development of modelling. It has been shown [4, 5] that the hybrid models provide an efficient tool to simulate plastic deformation behaviour and microstructure evolution during thermomechanical processing of metals, being based on more physical knowledge than either empirical models or neural network models alone.

The aim of the present work is to develop a hybrid model capable of predicting the flow behaviour as well as the recrystallisation characteristics and crystallographic texture evolution in an Fe-30wt%Ni austenitic model alloy deformed in hot plane

strain compression. The flow curves will be described as a function of the applied variables of strain rate and deformation temperature. The recrystallisation behaviour will be predicted from the measured microstructural state variables of internal dislocation density, subgrain size and misorientation between subgrains. The evolution of both the deformation and recrystallisation texture will be modelled using a data driven approach, namely artificial neural networks (ANN).

2. Experimental Procedure

The material used is Fe-30wt%Ni based austenitic model alloy with a chemical composition of 0.092wt% C, 0.19% Si, 1.67% Mn, 0.009% P, 0.003% S, 30.3% Ni, 1.51% Mo and the balance Fe. Specimens with dimensions of 60×30×10 mm were subjected to hot plane strain compression (PSC) testing using a computer controlled thermomechanical compression machine [6]. The specimens were preheated at 1250°C for 15 min air cooled and deformed at temperatures of 850, 950 and 1050°C and strain rates of 0.1, 1 and $10s^{-1}$ to a true strain level of approximately 0.7. In addition, for the deformation temperature of 950ºC and strain rates of 0.1 and 10 s^{-1} the deformation was interrupted at true strain levels of approximately 0.2, 0.4, 0.6 in order to study the microstructure evolution during straining. The mean recrystallised grain size obtained after preheating was about 120 μm. After testing, the PSC specimens were quenched in water within about 1 sec. Investigation of the grain structure, crystallographic texture and dislocation substructure was undertaken in the central areas of PSC specimens on sections containing the extension and normal sample directions, using quantitative light microscopy, electron backscatter diffraction (EBSD) and transmission electron microscopy (TEM) techniques. EBSD study was performed using an FEI Sirion field-emission gun scanning electron microscope, equipped with the HKL Technology EBSD attachment, operated at 15 kV. The corresponding data acquisition and processing were carried out using the HKL Channel 5 software. TEM examination of thin foils was performed using a Philips EM 420 microscope operated at 120 kV.

The crystallographic texture was measured for the specimens deformed at a temperature of 950ºC at strain rates of 0.1 and 10 s^{-1} using the EBSD technique [7].

The texture was represented by a three dimensional orientation distribution function (ODF) in the Euler space [7, 8]. The experimental ODFs were calculated in the Channel 5 software via superimposing Gaussian spreads of half-width of 5° on the measured individual orientations, utilizing the angular notation suggested by Bunge [8]. The deformation and recrystallisation textures were determined separately as a function of strain [6].

3. Flow Behaviour Modelling

The results of the PSC tests were analysed using standard procedures [9] to obtain equivalent true stress - equivalent true strain curves shown in Fig. 1. The instantaneous temperatures during deformation were calculated using a finite difference package based on the dimensions of the specimens, the deformation conditions and the heat transfer to the tools and environment [10]. The calculations assumed a specific heat capacity of 456 J Kg^{-1} K^{-1} and material density of 7700 kg m^{-3}. The temperature rise during deformation is shown in Fig. 2 for the different deformation conditions.

The curves in Figs. 1 and 2 were utilised to develop the model for the stress – strain behaviour based on the initial flow stress (σ_o), the stresses at a strain of 0.1 ($\sigma_{0.1}$), the steady state stress expected for work hardening and dynamic recovery only ($\sigma_{ss(e)}$) and the experimental steady state stress (σ_{ss}). These stresses were read directly from the curves and were plotted against the logarithm of the Zener Hollomon parameter

$$Z = \dot{\varepsilon} \exp(\frac{Q}{RT}) \tag{1}$$

where

       R is the gas constant (*R=8.31 J/mol K*)

       T is the temperature is Kelvin

       Q is the activation energy (*Q = 480 kJ/mol)* [6]

The temperature is the actual value for the strain of interest, which gives the instantaneous values of Z shown in Fig. 3. Over the whole range of Z, the curves in Fig.3 were fitted by the following general equation

$$\sigma = \frac{\sinh^{-1}(Z/A)^{(1/n)}}{\alpha} \qquad (2)$$

where n, A and α are constants obtained from the optimised curves, to give the values summarized by the following equations:

$$\sigma_0 = \frac{\sinh^{-1}(Z/1.54E18)^{(1/10.63)}}{0.0127} \qquad (3)$$

$$\sigma_{0.1} = \frac{\sinh^{-1}(Z/1.0E18)^{(1/7.91)}}{0.0075} \qquad (4)$$

$$\sigma_{ss(e)} = \frac{\sinh^{-1}(Z/2.27E18)^{(1/5.25)}}{0.0065} \qquad (5)$$

$$\sigma_{ss} = \frac{\sinh^{-1}(Z/0.87E18)^{(1/3.39)}}{0.0097} \qquad (6)$$

It was assumed that these equations are mechanical equations of state, so that the stress – strain curves expected for isothermal deformation (i.e. constant Z) conditions could be calculated and fitted to the equations

$$\sigma' = \sigma_0 + (\sigma_{ss(e)} - \sigma_0)[1 - \exp(\frac{-\varepsilon}{\varepsilon_r})]^{1/2} \qquad (7)$$

which applies for all strains when $\sigma_{(ss)e} = \sigma_{ss}$, but only for $\varepsilon \leq 0.7\varepsilon_p$ when $\sigma_{ss} < \sigma_{(ss)e}$. In the latter case

$$\sigma = \sigma' - 1.0(\sigma_{ss(e)} - \sigma_{ss})\left\{1 - \exp\left[-0.56\left((\frac{\varepsilon - 0.7\varepsilon_p}{\varepsilon_{ss}(e) - 0.7\varepsilon_p})\right)^{0.632}\right]\right\} \qquad (\varepsilon \geq 0.7\varepsilon_p) \qquad (8)$$

In equation (7), $\varepsilon_r = \varepsilon_{ss(e)}/2.3$ [11], where $\varepsilon_{ss(e)}$ is defined as the strain at which $(\sigma - \sigma_o) = 0.95(\sigma_{ss(e)} - \sigma_o)$ under isothermal conditions. In equation (8), ε_p is the strain at the peak stress when $\sigma_{ss} < \sigma_{(ss)e}$ under isothermal conditions. From optimised fits to these equations

$$\varepsilon_{ss(e)} = 11.8 \times 10^{-3} \, Z^{0.075} \qquad\qquad\qquad\qquad (9)$$

and

$$\varepsilon_p = 0.982 \times 10^{-5} Z^{0.23} \qquad\qquad (\varepsilon_{ss(e)} \geq 0.7 \varepsilon_p) \qquad (10)$$

The stress – strain curves computed for isothermal conditions are shown in Fig.4. It should be noted that the stress scale in this figure has been changed because of the major effect of the temperature rise on the experimental curves. It is noteworthy that the optimised values of $\varepsilon_{ss(e)}$ and ε_p cross over as the value of Z increases. It is considered that when the critical strain for the onset of dynamic recrystallisation ε_c (ε_c = 0.7 ε_p) becomes larger than the strain due to the onset of the steady state by work hardening and dynamic recovery only ($\varepsilon_{ss(e)}$), dynamic recrystallisation will not be nucleated.

Using these modelled values for the constants in equation (7) and (8), together with the computed temperature rise under the experimental conditions, leads to the curves in Fig.5. It can be seen that these are in good agreement with the experimental points for all the experimental conditions.

4. Recrystallisation Modelling

The physically-based models used in the present paper have been described in detail elsewhere [12, 13]. In order to have the inputs for the deformed microstructures, the mean values of subgrain size, δ, and the misorientation across subgrain boundaries, θ, were determined from the EBSD measurements of specimens deformed at 950°C and strain rates of 0.1 and 10 s^{-1} to different strains and water quenched. Measurements were made only in the unrecrystallised regions of the specimens and the results are shown in Fig. 6 (a) and (b). The austenite substructure was found to be rather heterogeneous and subgrains were frequently arranged in elongated "microbands" in agreement with the previously observed characteristics of hot deformed austenite [14, 15, 16, 17]. The internal dislocation structure present within the subgrain interiors was observed by transmission electron microscopy and was relatively high, but heterogeneous, densities were found for both strain rates at 950°C. The mean dislocation density values were not measured directly, but were estimated from the flow stresses, Fig. 1. From the results of changing strain rate tests, [18] it is expected

that the internal dislocation density, rather than the subgrain structure, determines the flow stress as

$$\sigma = \sigma_f + \alpha \, M \, G \, b \, \rho_i^{\frac{1}{2}} \tag{11}$$

where σ_f is the friction stress, assumed (arbitrarily) to account for half the flow stress for the present calculations, and M is the Taylor factor (3.1), G is the shear modulus (81×10^9). The resulting values of ρ_i are shown in Fig. 6 (c).

Only limited experimental data on recrystallisation are available for the specimens water quenched after a delay of about 1 s following deformation at 950°C and strain rates of 0.1 and 10 s^{-1} to different strains [6, 15]. Observations made at strains giving approximately the same fractions recrystallised at the two strain rates are shown in Fig. 7. There are too few data to be able to model the overall recrystallisation behaviour, but the procedure developed for modelling static recrystallisation of aluminium alloys [19, 20] can be applied to analyse the effects of the different deformation conditions at 950°C on the present Fe-30wt%Ni alloy. From physical metallurgy, the time for 50% static recrystallisation, t_{50}, is determined by the density of nucleation sites per unit volume, N_v, the stored energy per unit volume, P_D, and the grain boundary mobility, M_{gb}, as [21]

$$t_{50} = C \, N_v^{-\frac{1}{3}} \, P_D^{-1} \, M_{gb}^{-1} \tag{12}$$

where C is a numerical constant.

The experimental observations, Fig. 7, show clearly that grain boundaries are the preferred nucleation sites, and for the present initial grain size, d_o, and range of subgrain sizes, δ, nucleation at grain boundary surfaces is dominant, so the equation for nucleation density [21] can be simplified to

$$N_v = p_3 \, \lambda_3 \, S_v \, / \, \delta^2 \tag{13}$$

For deformation in plane strain compression the value of S_v increases with increase in equivalent strain, ε, as [21]

$$S_v = d_o^{-1} [0.429 \exp (- \sqrt{3}\varepsilon/2) + 0.571 + \exp (\sqrt{3}\varepsilon/2)] \qquad (14)$$

The stored energy depends on the dislocation density inside subgrains, ρ_i, the subgrain size, δ, and boundary misorientation, θ, as [21]

$$P_D = \frac{Gb^2}{10} \left[\rho_i \left(1 - \ln\left(10b\rho_i^{1/2}\right)\right) + \frac{2\theta}{b\delta}\left(1 + \ln\left(\frac{\theta_c}{\theta}\right)\right)\right] \qquad (15)$$

where G is the shear modulus (81×10^9), b is the Burgers vector (0.258×10^{-9} m) and θ_c is the critical angle for distinguishing a grain boundary and a subgrain boundary, and is assumed to be 15°.

The grain boundary mobility is not known, but it is assumed that its temperature dependence is given by

$$M_{gb} = M_{gbo} \exp (- Q/RT) \qquad (16)$$

where M_{gbo} is a constant, Q is the activation energy for boundary migration, which, by analogy with observations on the highly alloyed stainless steels, is assumed to be similar to the value for hot deformation, i.e. 480 kJ/mol.

Because of the unknown constants and the various assumptions made above, the calculated values of t_{50} have been normalised to $t_{50}*$ by dividing them by the value calculated for recrystallisation at 950^oC after deformation at 950^oC and a strain rate of 0.1 s^{-1} to a strain of 0.1. The resulting dependence of $t_{50}*$ on strain is shown in Fig. 8, in which the broken curves show the results, if there were no dynamic recrystallisation and annealing were carried out at 950^oC. At strain rates of both 0.1 s^{-1} and 10 s^{-1} the values of $t_{50}*$ decrease gradually with strain, by factors of 2.9 and 3.4 respectively, because of the effects of strain on S_v, δ, θ and ρ_i. However, by extrapolation in Fig. 2, deformational heating produces a temperature rise of about 12° and 52^oC by a strain of 0.8 at the two strain rates. In the short time before quenching, after which recrystallisation was observed, it can be assumed that annealing takes place at the final deformation temperature. The values of $t_{50}*$ given by the solid

curves now show major differences in the effects of strain at the two strain rates. At a strain rate of 0.1 s^{-1} the factor has increased slightly to 3.4, but at 10 s^{-1} it has increased to 18.

A quench delay time is sketched in by the chain line to cross the curve for 10 s^{-1} at approximately the strain when 50% recrystallisation was observed experimentally in the quenched specimens [6, 15]. Because the delay is about 1 s, this gives an absolute time scale for estimating t_{50}. At a strain rate of 0.1 s^{-1}, 1.7% recrystallisation is observed at a strain of 0.2. If this is the start of dynamic recrystallisation, it would be consistent with the curve for ε_p crossing the stress-strain curve for 950°C and 0.1 s^{-1} at a strain of 0.26, Fig. 4. By analogy with data on other steels in the austenitic condition [22], the time for 50% recrystallisation is expected to become independent of strain when dynamic recrystallisation has taken place. This is shown by the horizontal line labelled DRX in Fig. 8.

5. Crystallographic Texture Modelling

The starting texture of the material after heat treatment, as measured by EBSD, was rather weak, being characterised by the maximum of 1.7 times random (Fig. 9). For both the strain rates studied, the deformation texture was predominantly composed of orientations clustered around the copper {112}<111>, S {123}<634>, brass {011}<211> and Goss {011}<100> texture components [6, 15, 17]. There was also some limited presence of the cube {001}<100> components in the orientation distributions, in particular at a strain rate of 10 s^{-1}. The overall strength of the deformation texture gradually increased with strain and the relative intensities of the above main texture components varied as a function of strain. The recrystallisation textures were rather weak and consisted mainly of cube and brass components. An example of the measured ODFs after a strain of 0.6 is shown in Fig. 10(a) for deformation texture and in Fig 10(b) for recrystallisation texture.

In order to model the texture evolution, a systems modelling approach has been introduced to replicate the Taylor equation in the modelling framework for texture prediction. The approach is based on a data-driven systems modelling technique, which utilises experimental data for individual orientations with their deformation

conditions (temperature and strain) and models the rotations of these orientations using neural networks [23], as schematically illustrated in Fig. 11. The neural network model has been trained using experimental data points represented by the measured deformation or recrystallisation texture orientations (Euler angle triplets φ_1, Φ, φ_2) related to a particular strain and temperature and the corresponding starting texture orientations. With a single hidden layer of 50 neurons in a feed-forward, back-propagation network the system was trained for 50 epochs. Two networks have been trained, the first for the deformation texture and the second for the recrystallisation texture as a function of strain. Fig. 12 shows the modelled deformation and recrystallisation textures after a strain of 0.6, for direct comparison with Fig. 10. It can be seen that the model is able to capture all the important features of the experimentally obtained ODFs.

6. Discussion

As shown in the section on Flow Behaviour Modelling, in defining the values of strain to steady state ($\varepsilon_{ss(e)}$), when dynamic recovery is controlling, and of strain to the peak stress (ε_p), when dynamic recrystallisation takes place, it is important to derive the stress – strain curves for isothermal conditions to eliminate the effects of temperature rise, which differ for the different strain rates, see Fig. 2. When the values of these critical strains are superimposed on the stress – strain curves, Fig. 4, it can be seen that the critical strains cross over at a value of $Z = 2.5 \times 10^{22}$ s^{-1}. The simple interpretation of the cross-over is that at higher values of Z there will be no dynamic recrystallisation, but at lower values of Z dynamic recrystallisation will reduce the steady state stress by increasingly significant amounts as Z decreases. This is consistent with the changing shape of the stress – strain curves in Figs. 1 and 4, and as discussed later, with the microstructural observations of recrystallisation.

The experimental work is based on PSC tests in which the strain and strain rate distributions are characteristically heterogeneous [24]. This means that the local strain rate and accumulated strain on the active slip line fields differ from the nominal strain values calculated from the changes in specimen geometry. This has the consequence that equivalent stress (nominal) equivalent strain curves, as shown in Figs. 1, 4 and 5 have a dependence on the initial specimen geometry as well as on the material

properties. From finite element modelling [24] a correction procedure has been developed to relate the flow stress to the slip line field strain rate and strain [25]. This modifies the stress strain curves and eliminates the geometry effect, so that the corrected curves give constitutive equations that reflect the true material behaviour and can be applied accurately in modelling any type of hot deformation process. Equations (3 – 6) and (9, 10) have been corrected using the above procedure, and the new parameters (SLF correction) are compared with the original ones (no correction) in Table 1.

Table 1: Slip line field corrections.

variable	No correction			SLF correction		
	A	α	n	A	α	n
σ_0	1.54E18	0.0127	10.63	1.54E18	0.0111	11.68
$\sigma_{0.1}$	1.0E18	0.0075	7.91	1.0E18	0.0082	6.61
$\sigma_{ss(e)}$	2.27E18	0.0065	5.25	2.27E18	0.0068	4.98
σ_{ss}	0.87E18	0.0097	3.39	0.87E18	0.0108	3.43

From optimised fits to these equations

$$\varepsilon_{ss(e)(SLF)} = 12.1 \times 10^{-3} \, Z^{0.074} \tag{17}$$

and

$$\varepsilon_{p(SLF)} = 0.992 \times 10^{-5} Z^{0.23} \qquad (\varepsilon_{ss(e)} \geq 0.7\varepsilon_p) \tag{18}$$

The analysis of the normalised time for 50% recrystallisation in Fig. 8 is particularly relevant for interpreting the limited experimental data on recrystallisation observed in specimens quenched after about 1 s following the end of deformation. For a strain rate of 0.1 s^{-1}, the t$_{50}$ line for recrystallisation after dynamic recrystallisation is at a time more than an order of magnitude longer than the quench delay time (i.e. about 11 s). If the Avrami coefficient is 2, this means that negligible static or metadynamic recrystallisation is expected before quenching, and the fine grains observed experimentally are the dynamically recrystallised grains. This conclusion appears to be consistent with the EBSD and TEM observations showing evidence of substructure within the recrystallised grains [15]. The fraction of dynamic recrystallisation increases with increasing strain as expected from the stress – strain curve.

After deformation at a strain rate of 10 s^{-1}, from the ratios of t_{50}* at strains of 0.2 and 0.8 to the quench delay time, the expected statically recrystallised fractions (if the Avrami coefficient is 2) are 5% and 97%, respectively, in reasonable agreement with the observed values of 2.3% and 100% [6, 15]. The physically based model therefore provides a semi-quantitative interpretation of the limited recrystallisation data presently available.

For both the strain rates studied, the deformation texture evolution with increasing strain was characterised by gradual crystallite rotations towards the stable end texture components located along both the α and β fibres in the Euler space [8], as expected for PSC deformation of f.c.c. metallic materials largely occurring via crystallographic slip [7, 26, 27].

Different techniques have been used to model the grain rotations during plastic deformation, and thus to predict deformation texture evolution, each having its limitations and constraints [28]. Recrystallisation texture has been modelled separately using different principles [27]. In the present work, a different approach is introduced based on a data-driven systems modelling technique, which utilises experimental data for individual orientations with their deformation conditions, and models the rotations of these orientations using neural networks [23]. Such a technique does not depend on the finite element method to produce the deformation conditions which is time consuming. The data generated (>3000 points) from the measured textures is utilised to train the ANN so that the texture evolution can be predicted in a much shorter time. Another advantage of the present modelling technique is that both the deformation and recrystallisation texture evolution can be predicted using a common approach.

7. Conclusions

A hybrid modelling technique, which utilises a combination of empirical, physically-based and neuro-fuzzy models, has been developed in the present work. The hybrid model has been successfully applied to predict the flow behaviour, recrystallisation characteristics and crystallographic texture evolution in a Fe-30wt%Ni austenitic

model alloy subjected to hot plane strain compression. The flow behaviour has been described as a function of the applied variables of strain rate and temperature using an empirical model. The recrystallisation characteristics have been predicted from the measured microstructural state variables of internal dislocation density, subgrain size and misorientation between subgrains using a physically-based model. The evolution of both deformation and recrystallisation texture has been modelled using artificial neural networks. The hybrid modelling approach adopted in the present work, which combines physical equations, adaptive numeric modelling, optimisation and metallurgical knowledge, provides a promising tool for modelling industrial hot-working processes in the future.

8. Acknowledgments

References

1. Almaguer S, Sellars CM, Rainforth WM. In: Gottstein G, MolodovDA, editors. Proc. 1st Joint Int. Conf. on Recrystallisation and Grain Growth, Aachen, Springer-Verlag, 2001;2:p.831.

2. Swartzendruber LJ, Itkin VP, Alcock C. Journal of Phase Equilibria, 1991;12:288-312.

3. Charnock W, Nutting J. Metal Science Journal, 1967;1:123-7.

4. Abbod MF, Talamantes-Silva J, Zhu Q, Linkens DA. In: de Silva CW, Karray F, editors. Proceedings of the 2002 IEEE International Symposium on Intelligent Control (ISIC2002), Vancouver, British Columbia, Canada, 27–30 October. Omnipress: IEEE Control Systems Society; 2002. p. 321–6.

5. Abbod MF, Linkens DA, Zhu Q. Materials Science and Engineering A, 2002;A333:397-408.

6. Bai F. Microstructural evolution in a model Fe-30Ni alloy during plane strain compression, PhD Thesis, University of Sheffield, April 2005.

7. Randle V, Engler O. Introduction to Texture Analysis: Macrotexture, Microtexture and Orientation Mapping, Gordon and Breach Science Publishers, Amsterdam 2000.

8. Bunge HJ. Texture Analysis in Materials Science: Mathematical Methods, Butterworths, London 1982.

9. Loveday MS, Mahon GJ, Roebuck B, Lacey AJ, Palmiere EJ, Sellars CM, van der Winden MR. Mats at High Temperatures, 2006;23**:**85–118.

10. Hand RJ, Foster SR, Sellars CM. Mat. Sci. and Tech, 2000;16:442-50.

11. Shi H, McLaren AJ, Sellars CM, Shahani R, Bolingbroke R. Mater Sci Technol, 1997;13:210.

12. Zhu Q, Shercliff HR, Sellars CM. In: Chandra T and Sakai T, editors, Proc. of the Int. Conf. on Thermomechanical Processing of Steels and Other Materials (THERMEC'97), Wollongong/Australia, TMS, 1997; p.2039.

13. Sellars CM, Zhu Q. Materials Science and Engineering, 2000;A280:1-7.

14. Bai F, Cizek P, Palmiere EJ, Rainforth WM, Beynon JH. Materials Science Forum, 2003;426-432:3623-3628.

15. Bai F, Cizek P, Palmiere EJ, Rainforth WM. Materials Science Forum, 2004;467-470:21-26.

16. Cizek P, Whiteman JA, Rainforth WM, Beynon JH, Microsc J., 2004;213:285-95.

17. Cizek P, Bai F, Palmiere EJ, Rainforth WM. J. Microsc., 2005;217:138-151.

18. Castro Fernandes FR, Sellars CM, Whiteman JA. Mats. Sci. and Technol., 1990;6:453-60.

19. Zhu Q, Abbod MF, Talamantes-Silva J, Sellars CM, Linkens DA, Beynon JH. Acta Mater., 2003;51:5051–62,

20. Abbod MF, Sellars CM, Linkens DA, Zhu Q, Mahfouf M. Mats. Sci. and Eng., 2005;A395:901-11.

21. Sellars CM, Zhu Q. Materials Science and Engineering, 2000;A280:p.1-7.

22. Sellars CM. In: Sellars CM, Davies GJ, editors. Conf on Hot Working and Forming Processes, Metals Soc., London, 1980;3–15.

23. Nørgaard M, Neural Networks for Modelling and Control of Dynamic Systems, Springer 2000.

24. Mirza MS, Sellars CM. Materials Science and Technology, 2001;17:1133-41.

25. Kowalski B, Lacey AJ, Sellars CM. Mats. Sci. and Tech., 2003;19:1564.

26. Hirsch J, Lücke K. Acta Metall., 1988;36:2863.

27. Humphreys FJ, Hatherly M, *Recrystallisation and Related Annealing Phenomena*, Pergamon, Oxford 1996.

28. Kocks UF, Tome CN, Wenk HR, Texture and Anisotropy: Preferred Orientations in Polycrystals and their Effects on Materials Properties, Cambridge University Press 1998.
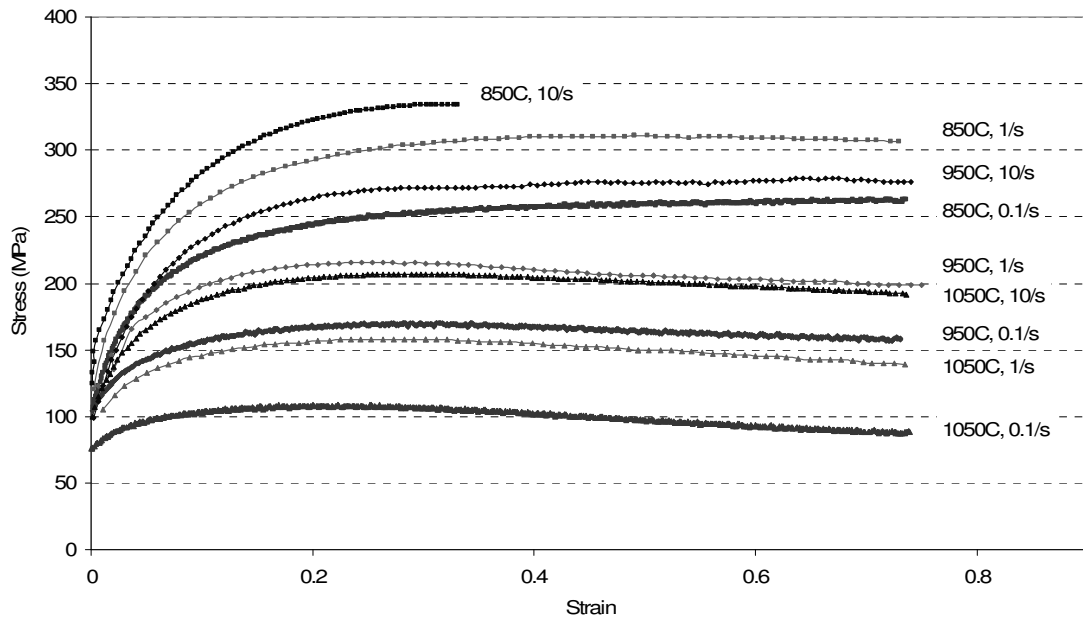
Figure 1: Experimental equivalent stress-equivalent strain curves for different deformation conditions.
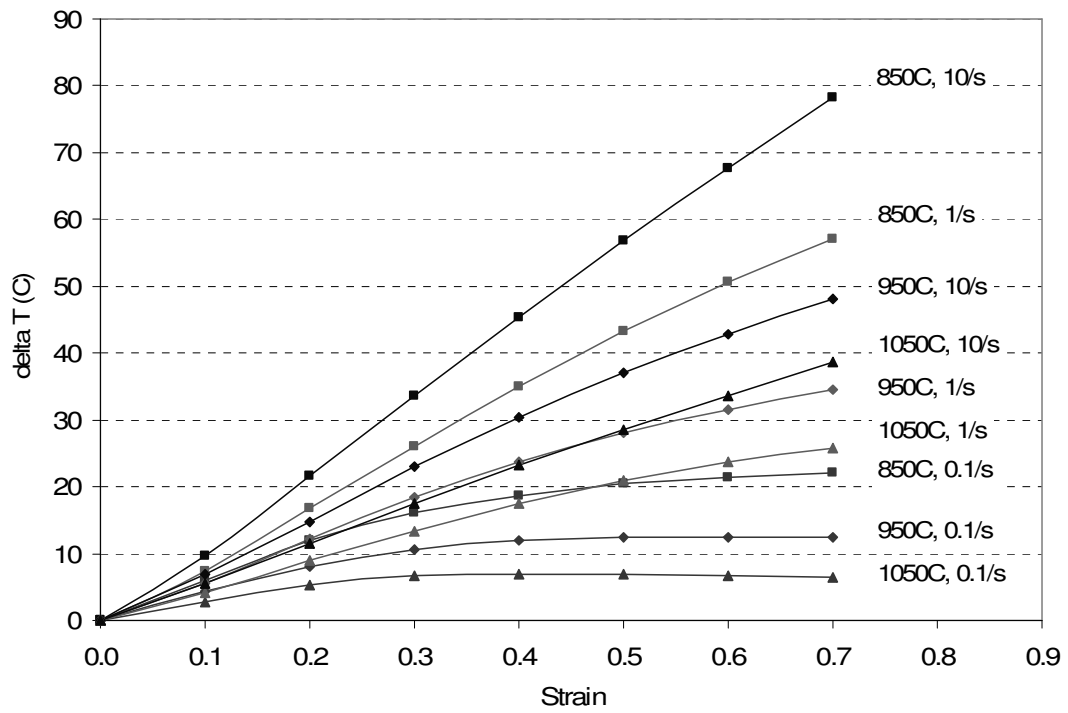
Figure 2: Calculated temperature rise due to deformational work done during PSC tests.
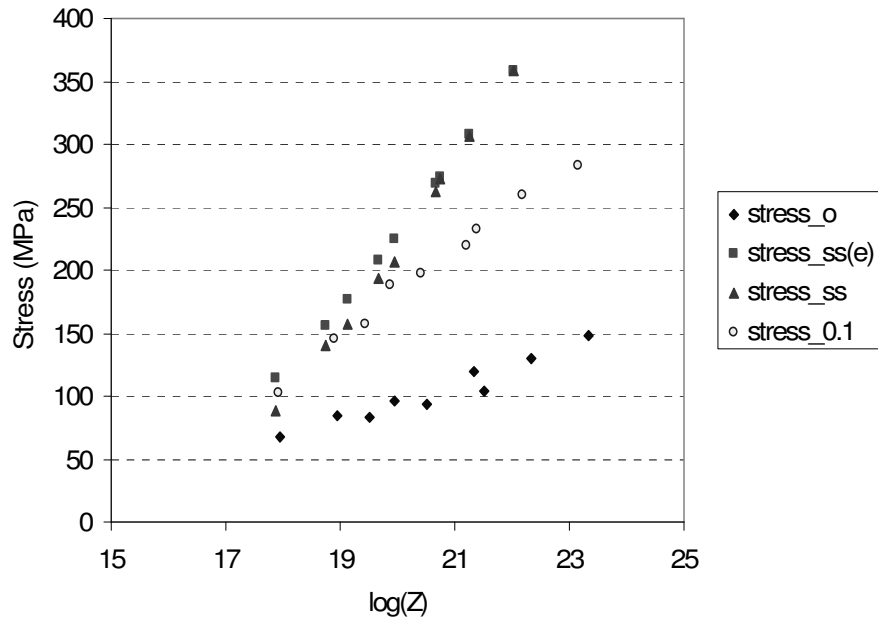
Figure 3: Measured stresses at different strains plotted against the logarithm of the instantanenous value of Zener Hollomon parameter.
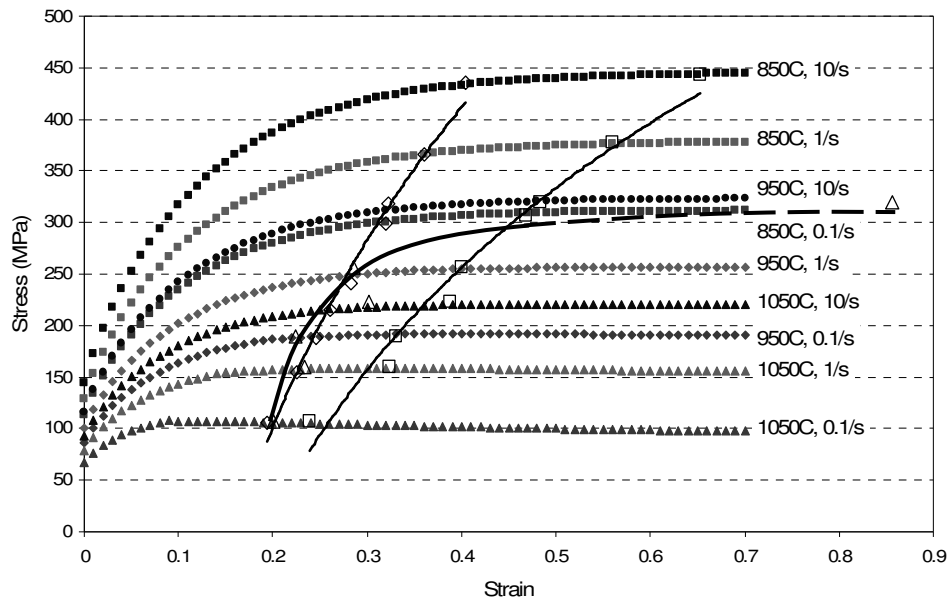
Figure 4: Stress - strain curves for isothermal conditions.
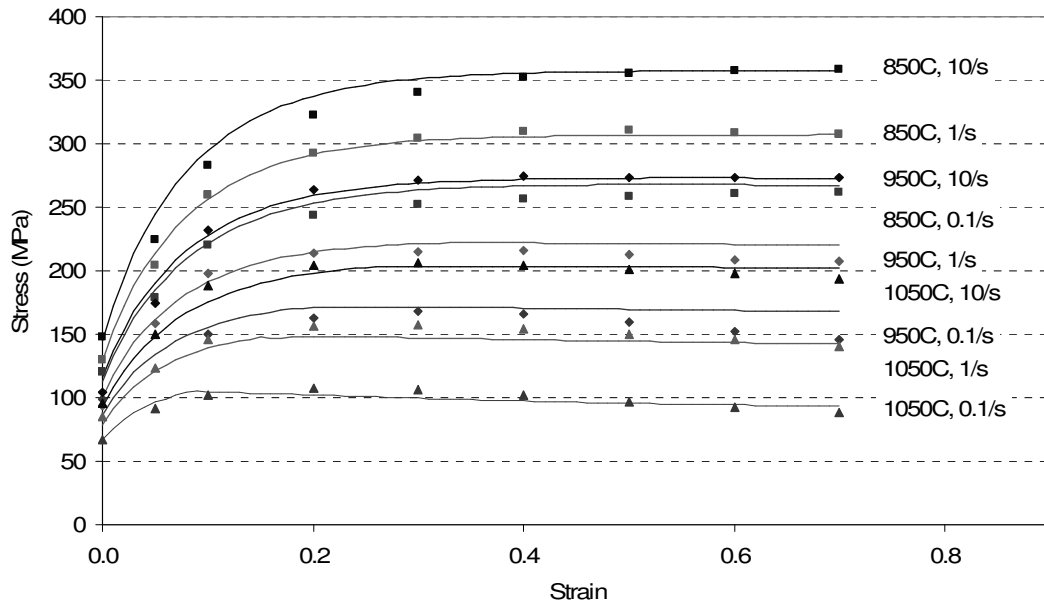
Figure 5: Experimental (points) and modelled (solid lines) stress – strain curves for
different deformation conditions.
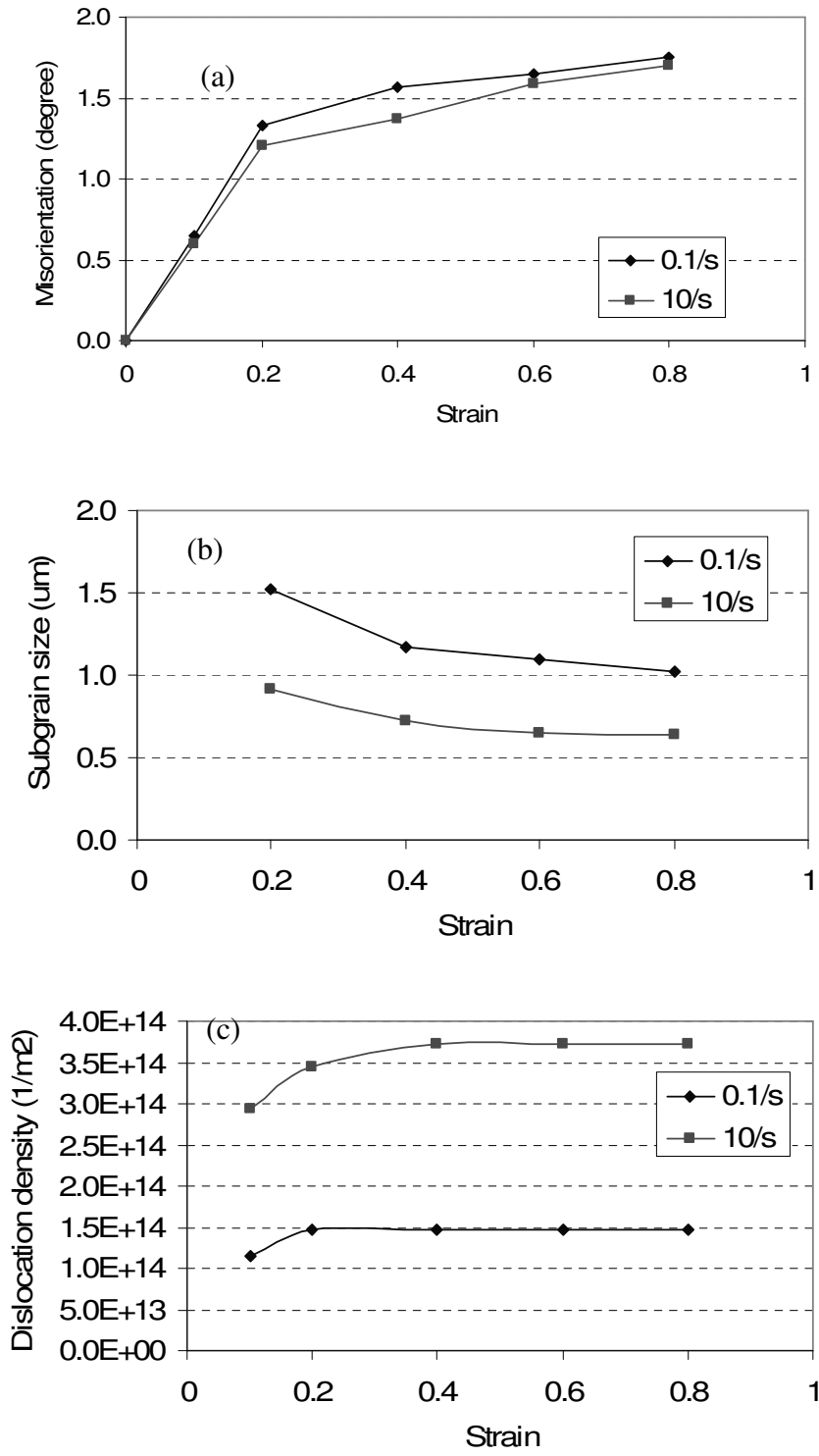
Figure 6. Internal states of specimens deformed at 950°C: (a) measured subgrain size, (b) measured subgrain boundary misorientation and (c) estimated internal dislocation density.
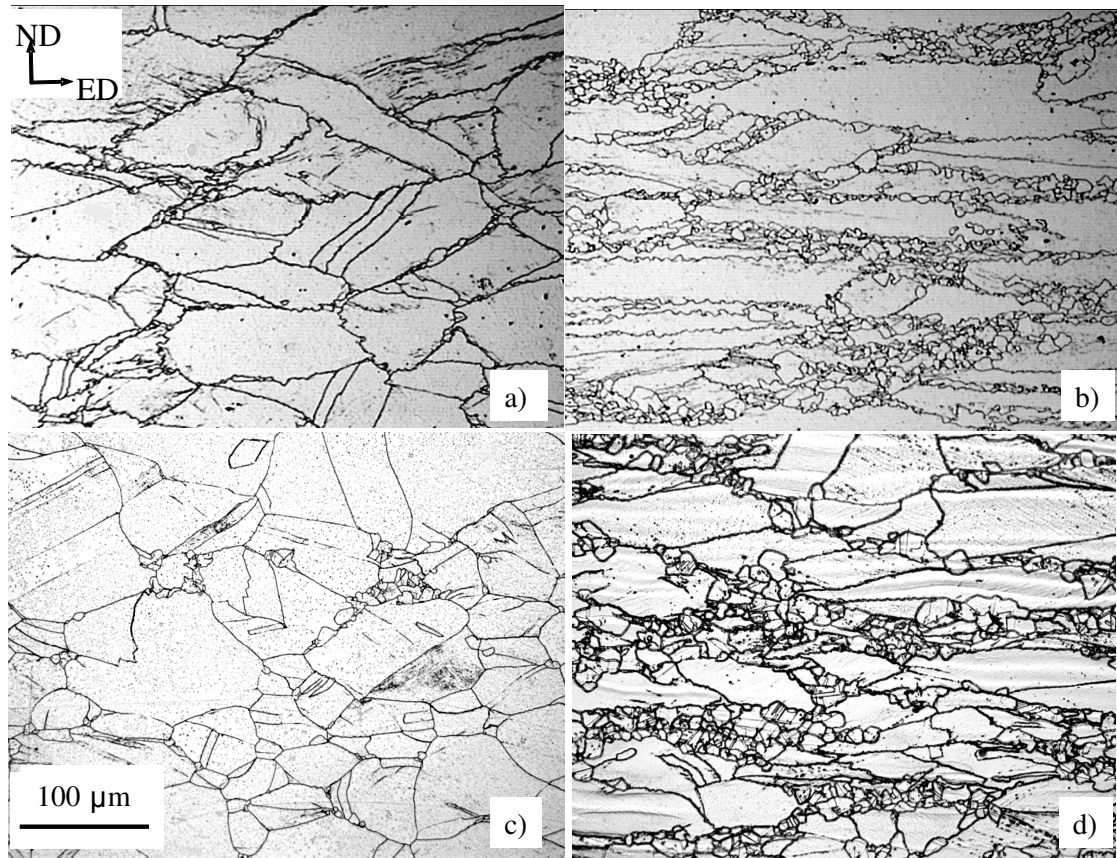
Figure 7: Optical micrographs showing the longitudinal section of PSC test specimens deformed at 950°C and a strain rate of 0.1 s^{-1} to strains of (a) 0.4 and (b) 0.8 and at a strain rate of 10 s^{-1} to strains of (c) 0.2 and (d) 0.6.
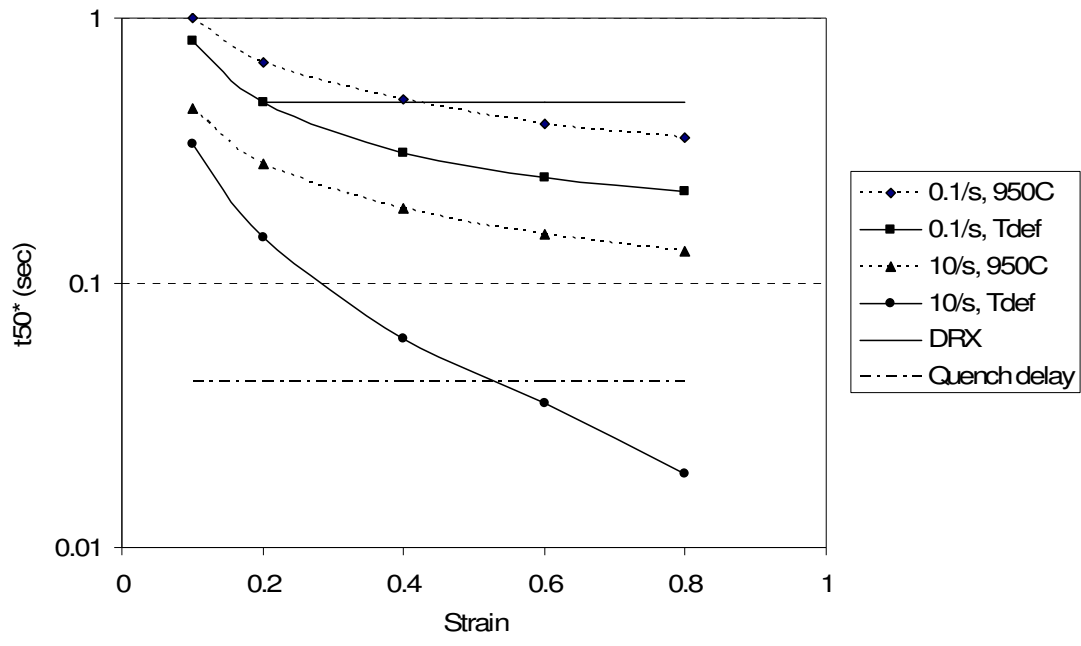
Figure 8: Normalised time for 50% recrystallisation for different deformation conditions.
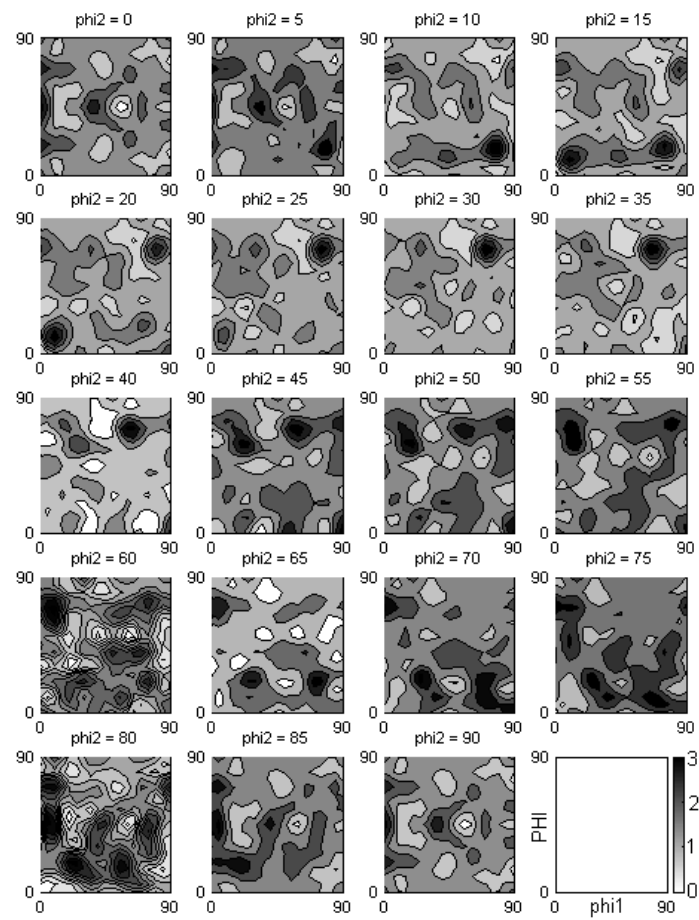
Figure 9: Initial crystallographic texture.
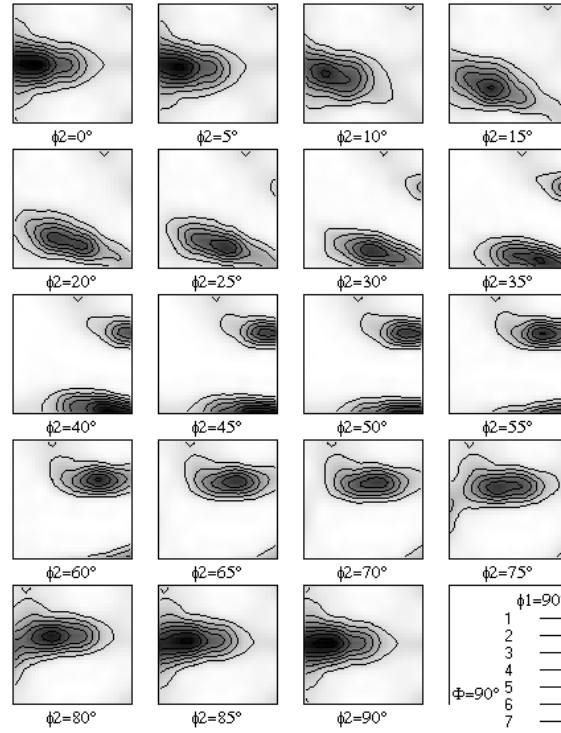
(a) Measured deformation texture @ ε = 0.6
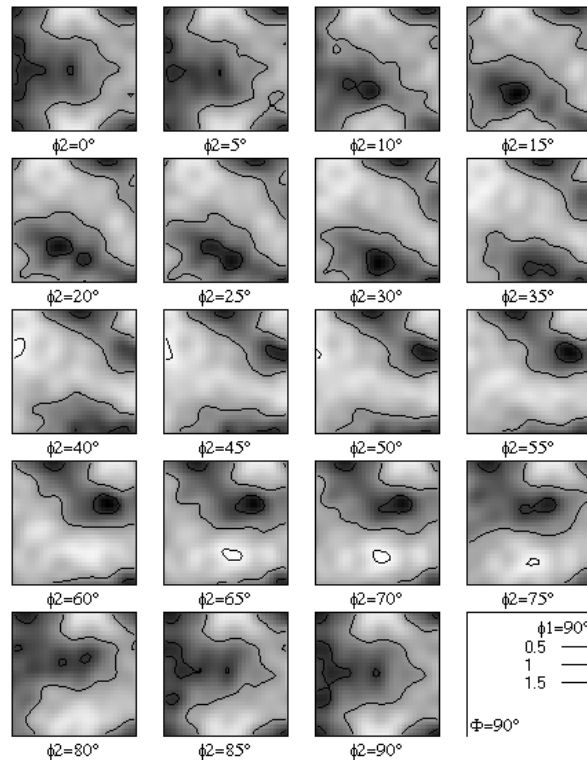
(b) Measured recrystallisation texture @ ε = 0.6

Figure 10: The evolution of deformation and recrystallisation texture determined using the EBSD technique and expressed by the orientation distribution function (ODF) in Bunge notation [8]: Deformation conditions: strain rate = 10/s, temperature = 950°C.
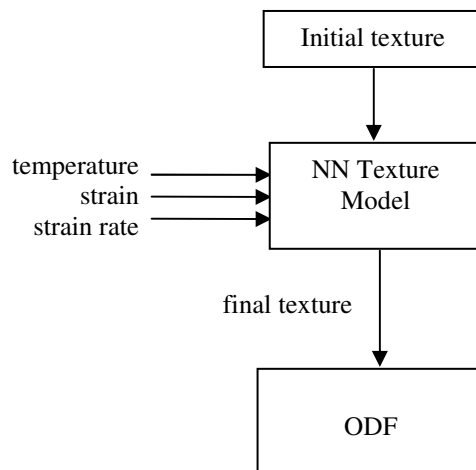
Figure 11: Systems approach texture model.
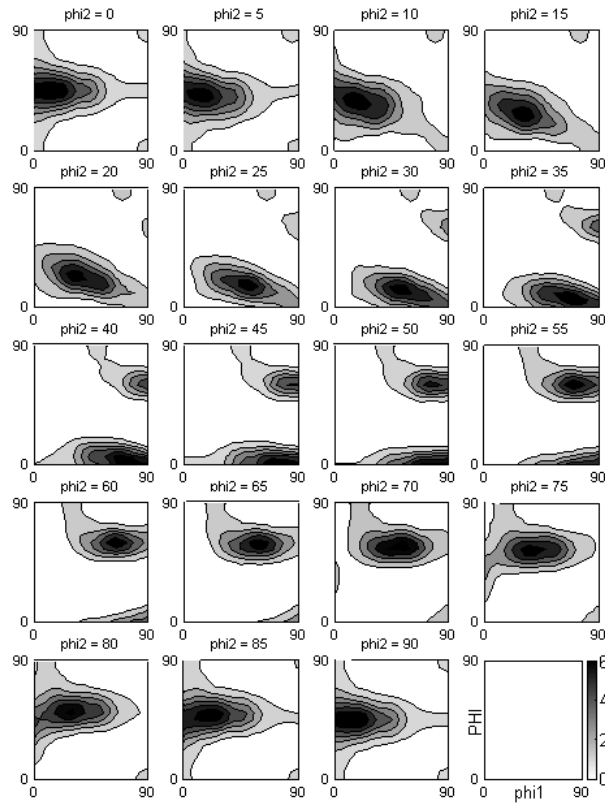
(a) Predicted deformation texture @ ε = 0.6
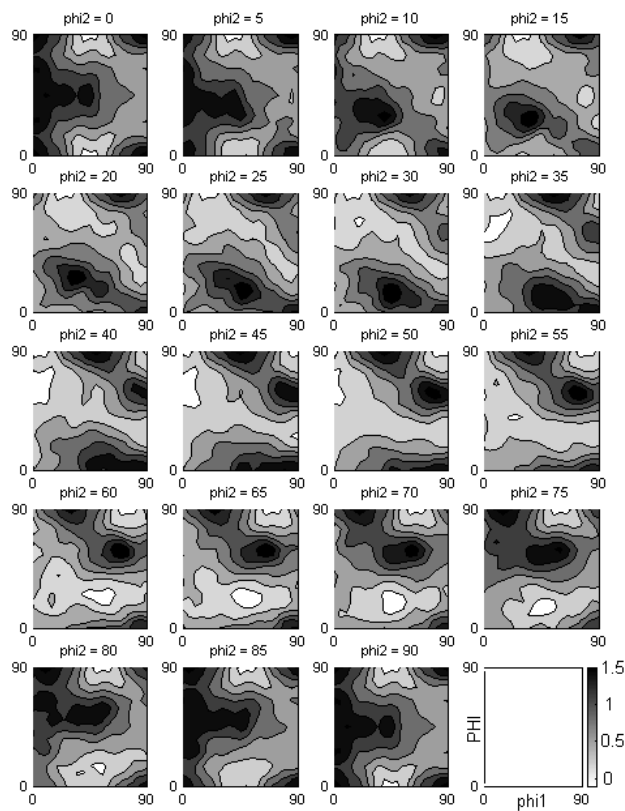
(b) Predicted recrystallisation texture @ ε = 0.6

Figure 12: Prediction via ANN of the evolution of deformation and recrystallisation texture expressed by the orientation distribution function (ODF) in Bunge notation [8]: Deformation conditions: strain rate = 10/s, temperature = 950°C.